23. See the supplementary materials on *Science* Online.
24. N. M. Marković, R. R. Adžić, B. D. Cahan, E. B. Yeager, *J. Electroanal. Chem.* **377**, 249–259 (1994).
25. M. D. Maciá, J. M. Campiña, E. Herrero, J. M. Feliu, *J. Electroanal. Chem.* **564**, 141–150 (2004).
26. X. Huang *et al.*, *Nat. Nanotechnol.* **6**, 28–32 (2011).
27. X. Xia, J. Zeng, Q. Zhang, C. H. Moran, Y. Xia, *J. Phys. Chem. C* **116**, 21647–21656 (2012).
28. L. Chen *et al.*, *Nano Lett.* **14**, 7201–7206 (2014).
29. V. Mazumder, S. Sun, *J. Am. Chem. Soc.* **131**, 4588–4589 (2009).
30. U.S. Department of Energy, Technical Plan: Fuel Cells (2016); www.energy.gov/sites/prod/files/2016/06/f32/fcto_myrdd_fuel_cells_0.pdf.
31. C. Roychowdhury *et al.*, *Chem. Mater.* **18**, 3365–3372 (2006).
32. J. K. Nørskov *et al.*, *J. Phys. Chem. B* **108**, 17886–17892 (2004).
33. V. Stamenkovic *et al.*, *Angew. Chem. Int. Ed.* **45**, 2897–2901 (2006).
34. X. Zhang, G. Lu, *J. Phys. Chem. Lett.* **5**, 292–297 (2014).
35. M. Mavrikakis, B. Hammer, J. K. Nørskov, *Phys. Rev. Lett.* **81**, 2819–2822 (1998).
36. P. Strasser *et al.*, *Nat. Chem.* **2**, 454–460 (2010).
37. L. Li *et al.*, *J. Phys. Chem. Lett.* **4**, 222–226 (2013).
38. D. F. van der Vliet *et al.*, *Nat. Mater.* **11**, 1051–1058 (2012).

ELECTROCATALYSIS

Ultrafine jagged platinum nanowires enable ultrahigh mass activity for the oxygen reduction reaction

Mufan Li,[1] Zipeng Zhao,[2] Tao Cheng,[3] Alessandro Fortunelli,[3,4] Chih-Yen Chen,[2] Rong Yu,[5] Qinghua Zhang,[6] Lin Gu,[6] Boris V. Merinov,[3] Zhaoyang Lin,[1] Enbo Zhu,[2] Ted Yu,[3,7] Qingying Jia,[8] Jinghua Guo,[9] Liang Zhang,[9] William A. Goddard III,[3]* Yu Huang,[2,10]* Xiangfeng Duan[1,10]*

Improving the platinum (Pt) mass activity for the oxygen reduction reaction (ORR) requires optimization of both the specific activity and the electrochemically active surface area (ECSA). We found that solution-synthesized Pt/NiO core/shell nanowires can be converted into PtNi alloy nanowires through a thermal annealing process and then transformed into jagged Pt nanowires via electrochemical dealloying. The jagged nanowires exhibit an ECSA of 118 square meters per gram of Pt and a specific activity of 11.5 milliamperes per square centimeter for ORR (at 0.9 volts versus reversible hydrogen electrode), yielding a mass activity of 13.6 amperes per milligram of Pt, nearly double previously reported best values. Reactive molecular dynamics simulations suggest that highly stressed, undercoordinated rhombus-rich surface configurations of the jagged nanowires enhance ORR activity versus more relaxed surfaces.

P latinum (Pt) represents the essential element for catalyzing the oxygen reduction reaction (ORR) (*1–3*). However, the high cost of Pt is the primary limiting factor preventing the widespread adoption of fuel cells that critically depend on ORR (*4, 5*). Therefore, higher Pt mass activity—the catalytic activity per given mass of Pt—must be achieved to reduce the required platinum usage. The Pt mass activity is determined by the specific activity (normalized by surface area) and the electrochemically active surface area (ECSA, normalized by mass). The specific activity can be optimized by tuning the chemical environment, including chemical composition (*6–9*), exposed catalytic surface (*1, 10–12*), and Pt coordination environment (*13–16*). To date, the highest specific activities have generally been achieved on single-crystal surfaces or well-defined nanoparticles (NPs) with specifically engineered facet structure and alloy compositions. For example, the Pt₃Ni (111) single-crystal facet (*1*) and Pt₃Ni octahedral NPs have been shown to exhibit ORR-favorable surface structure for greatly enhanced activity (*17–19*), but such alloys typically suffer from insufficient stability because of electrochemical leaching of Ni during electrochemical cycling, as well as decreased ECSA because of agglomeration of the NPs. Introduction of Mo surface dopants can mitigate such leaching processes and help maintain the ORR-favorable Pt₃Ni (111) surface for enhanced activity and stability (*19*). On the other hand, ECSA may be improved by tailoring the geometrical factors through the creation of ultrafine nanostructures (*20, 21*) or core/shell nanostructures with an ultrathin Pt skin (*22–24*) that exposes most Pt atoms on the surface. Although high surface areas have been achieved on these structures, the reported ECSA values for these optimized structures are typically limited to ~70 m²/g$_{Pt}$.

To boost Pt mass activity and Pt utilization efficiency, an ideal catalyst should have an ORR-favorable chemical environment for high specific activity, optimized geometric factors for high ECSA (*20–24*), and a mechanism to maintain these high values for long periods of operation. We report the preparation of ultrafine jagged Pt nanowires (J-PtNWs) with rich ORR-favorable rhombic configurations that lead to a specific activity of 11.5 mA/cm² [at 0.9 V versus RHE (reversible hydrogen electrode)] and an ECSA of 118 m²/g$_{Pt}$. Together, these J-PtNWs deliver a mass activity of 13.6 A/mg$_{Pt}$ (at 0.9 V versus RHE), which is ~50 times that of the state-of-the-art commercial Pt/C catalyst and nearly double the highest previously reported mass activity values of 6.98 A/mg$_{Pt}$ (*19*) and 5.7 A/mg$_{Pt}$ (*23*).

We prepared Pt/NiO core/shell nanowires by reducing platinum (II) acetylacetonate [Pt(acac)₂] and nickel(II) acetylacetonate [Ni(acac)₂] in a mixture solvent of 1-octadecene and oleylamine (*25*). Transmission electron microscopy (TEM) showed that the as-synthesized nanowires exhibit an apparent core/shell structure with a contrast of darker core and lighter shell. The nanowires have a typical overall diameter of ~5 nm or less, and a length of ~250 to 300 nm (Fig. 1A and fig. S1A). High-resolution TEM (HRTEM) confirmed the core/shell structure with a typical core diameter of 2.0 ± 0.2 nm (Fig. 1D). The shell shows well-resolved lattice fringes with a spacing of 0.24 nm,

[1]Department of Chemistry and Biochemistry, University of California, Los Angeles, CA 90095, USA. [2]Department of Materials Science and Engineering, University of California, Los Angeles, CA 90095, USA. [3]Materials and Process Simulation Center, California Institute of Technology, Pasadena, CA 91125, USA. [4]CNR-ICCOM, Consiglio Nazionale delle Ricerche, 56124 Pisa, Italy. [5]National Center for Electron Microscopy in Beijing, School of Materials Science and Engineering, Tsinghua University, Beijing 100084, P. R. China. [6]Institute of Physics, Chinese Academy of Sciences, Beijing 100190, P. R. China. [7]Department of Chemical Engineering, California State University, Long Beach, CA 90840, USA. [8]Department of Chemistry and Chemical Biology, Northeastern University, Boston, MA 02115, USA. [9]Advanced Light Source, Lawrence Berkeley National Laboratory, Berkeley, CA 94720, USA. [10]California NanoSystems Institute, University of California, Los Angeles, CA 90095, USA.
*Corresponding author. Email: wag@wag.caltech.edu (W.A.G.); yhuang@seas.ucla.edu (Y.H.); xduan@chem.ucla.edu (X.D.)

corresponding to the (111) interplanar distance of face-centered cubic (fcc) NiO (Fig. 1D), and the core displays a primary lattice spacing of 0.23 nm, corresponding to Pt (111) planes (Fig. 1D).

These Pt/NiO nanowires were then loaded onto carbon black and annealed in an argon/hydrogen mixture (Ar/H$_2$: 97/3) at 450°C to produce PtNi alloy nanowires. The overall morphology of the nanowire was maintained without obvious change in length or diameter, but the apparent core/shell contrast disappeared (Fig. 1B), suggesting the formation of uniform PtNi alloy nanowires. The HRTEM image of the annealed nanowire confirms a uniform contrast with a well-resolved lattice spacing of 0.21 nm throughout the entire nanowire diameter (Fig. 1E), consistent with the (111) lattice spacing of the PtNi alloy. This evolution, from the initial core/shell nanowires before annealing to uniform alloy nanowires after annealing, was also confirmed by high-angle annular dark-field scanning transmission electron microscope (HAADF-STEM) studies (fig. S1, C and D).

Our energy-dispersive x-ray (EDX) spectroscopy elemental analysis shows that the overall Pt/Ni ratio remained essentially the same (Pt/Ni: 15/85) before and after annealing (fig. S3, A and B). The EDX spectroscopy line scan profile of the as-prepared nanowires also confirms the core/shell structure with a Pt core (Fig. 1G) that diffuses homogeneously throughout the entire nanowire after annealing (Fig. 1H). X-ray diffraction (XRD) studies also confirm the evolution of the initial Pt/NiO core/shell configurations into a fully alloyed PtNi nanowire structure (fig. S4). Furthermore, x-ray photoelectron spectroscopy (XPS) studies demonstrate that the nickel valence state changed from Ni^{x+} in the Pt/NiO core/shell nanowires to mostly Ni^0 after annealing, consistent with the formation of PtNi alloy (fig. S5).

We believe that the nanowire geometry is essential for ensuring the thermal stability of these ultrafine nanowires under high-temperature annealing. For example, a similar thermal annealing process applied to ultrafine PtNi NPs led to substantial aggregation of the NPs (a size increase from ~7 nm to aggregates of 10 to 30 nm) (fig. S2), which could be partly attributed to the movement and fusion of NPs. In contrast, nanowires supported on carbon black have multiple anchoring points and their mobility is much lower than that of NPs with a single point contact on a carbon support.

We used an electrochemical dealloying (leaching) process to gradually remove Ni atoms from the PtNi alloy nanowires, which allowed the rearrangement of Pt atoms on the surface to form the J-PtNWs. We performed cyclic voltammetry (CV) in N$_2$-saturated 0.1 M HClO$_4$ solution (0.05 V to 1.1 V versus RHE) with a sweep rate of 100 mV s^{-1} (Fig. 2A). With the CV curves, the ECSA$_{H_{upd}}$ was derived from the H$_{upd}$ adsorption/desorption peak areas (0.05 V < E < 0.35 V) normalized by the total mass of the loaded Pt. The PtNi alloy nanowires initially showed an essentially negligible ECSA$_{H_{upd}}$ during the first CV cycle. The ECSA$_{H_{upd}}$ increased steadily with the increasing number of

CV cycles (Fig. 2B). The nanowires were fully activated in ~160 CV cycles to reach a stable ECSA$_{H_{upd}}$ up to 118 m^2/g$_{Pt}$, whereas the previous highest reported values were ~70 m^2/g$_{Pt}$ (Table 1).

Structural and elemental studies were performed to characterize the fully activated nanowires after CV cycles. Low-resolution TEM images show that the overall nanowire structure was well maintained
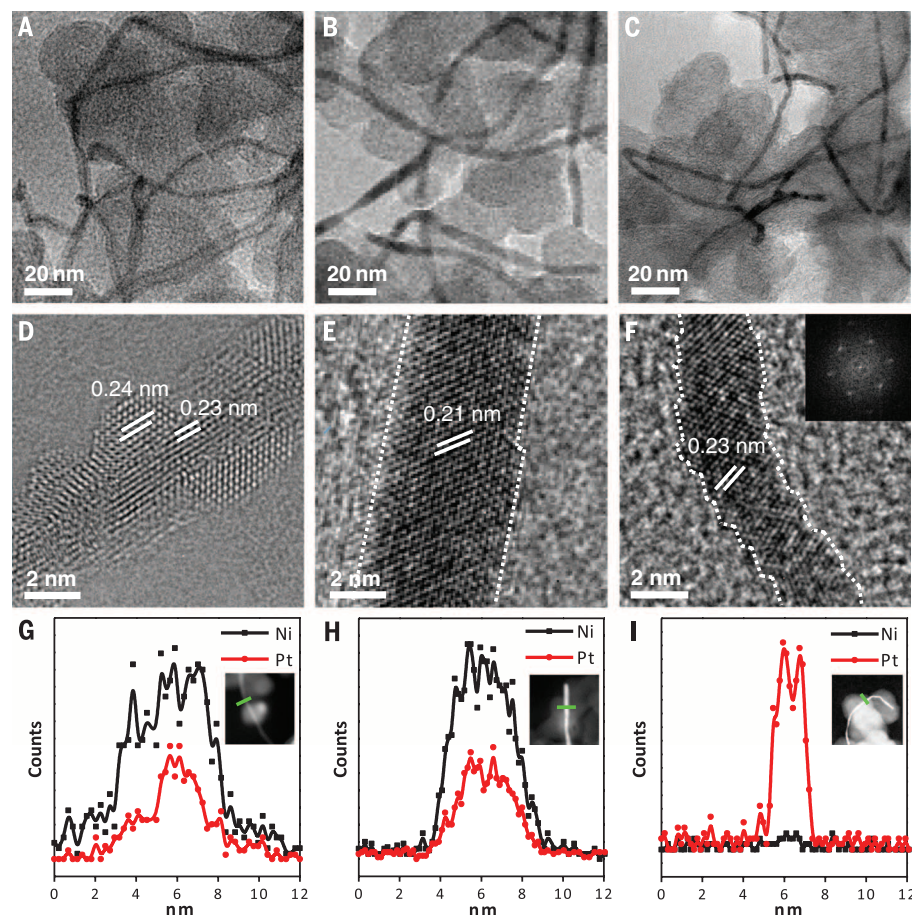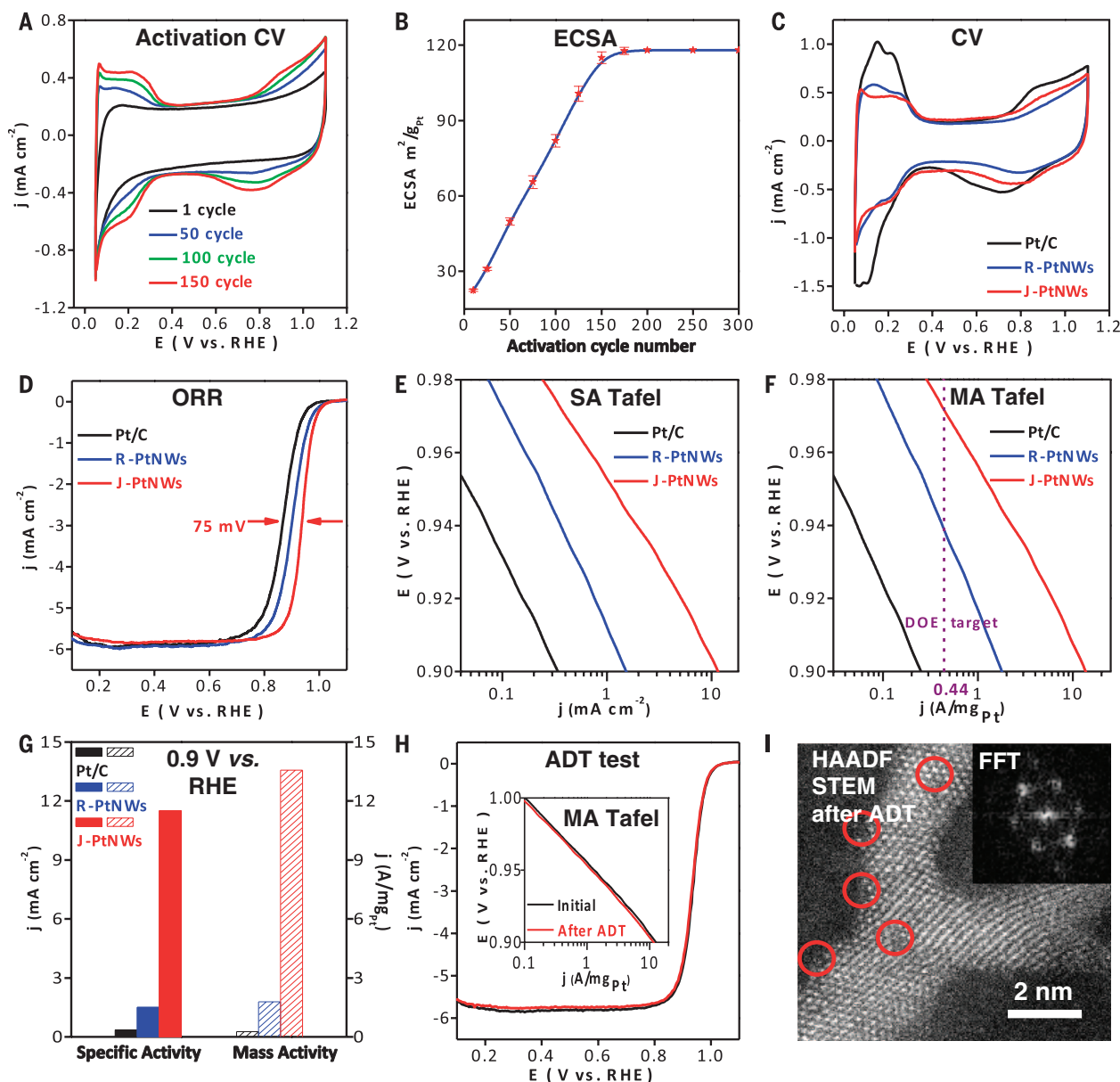

Fig. 1. Structure and composition characterization of different stages of the J-PtNW evolution process. (**A** to **F**) Representative TEM images (A to C) and HRTEM images (D to F) of the Pt/NiO core/shell nanowires, the PtNi alloy nanowires, and the J-PtNWs supported on carbon, respectively. The inset in (F) shows the corresponding FFT image. The dashed lines in (E) and (F) show the outline of the nanowires, highlighting the rough surface of the J-PtNWs. (**G** to **I**) EDX spectroscopy line-scan profiles of the corresponding nanowires show clearly the evolution from the Pt/NiO core/shell to PtNi alloy and then to pure PtNWs.

Table 1. Electrochemically active surface area (ECSA), specific activity, half-wave potential, and mass activity of J-PtNWs/C, R-PtNWs/C, and Pt/C catalysts, in comparison to those in several representative recent studies. NA, not applicable.

	ECSA (m^2/g$_{Pt}$)	Specific activity (mA/cm^2) at 0.90 V	Half-wave potential (V)	Mass activity at 0.90 V	(A/mg$_{Pt}$) at 0.935 V
J-PtNWs/C (this work)	118	11.5	0.935	13.6	2.87
R-PtNWs/C (this work)	110	1.59	0.899	1.76	0.5
Pt/C (this work)	74	0.35	0.860	0.26	0.06
Octahedron Pt$_{2.5}$Ni/C (17)	21	NA	NA	3.3	NA
Nanoframe Pt$_3$Ni/C (23)	67.2	NA	NA	5.7	NA
Mo-Pt$_3$Ni/C (19)	67.7	10.3	NA	6.98	NA
DOE 2017 target	NA	NA	NA	0.44	NA

Fig. 2. Electrochemical performance of the jagged PtNWs (J-PtNWs) versus regular synthetic PtNWs (R-PtNWs) and commercial Pt/C catalyst. (**A**) Cyclic voltammetry (CV) curves corresponding to different activation cycles of the dealloying process, clearly indicating the increasing surface area with increasing number of CV cycles. (**B**) The evolution of ECSA with increasing number of CV cycles, showing that 160 cycles are sufficient to construct the J-PtNW and reach a stable ECSA. (**C** and **D**) CV and ORR polarization curves for the J-PtNWs, R-PtNWs, and Pt/C catalyst, respectively. (**E** and **F**) Specific activity (SA) and mass activity (MA) Tafel plot for the J-PtNWs, R-PtNWs, and Pt/C catalyst, respectively. The purple dashed line indicates the 2017 mass activity target (at 0.90 V versus RHE) set by DOE. (**G**) Comparison of specific activities and mass activities of the J-PtNWs, R-PtNWs, and Pt/C catalyst at 0.9 V versus RHE, showing that the J-PtNWs deliver 33 times the specific activity or 52 times the mass activity of the Pt/C catalyst. (**H**) ORR polarization curves and mass activity Tafel plot (inset) for the J-PtNWs before and after 6000 CV cycles between 0.6 and 1.0 V versus RHE, showing little loss in activity. The scan rate for the accelerated durability test (ADT) is 100 mV s^{-1}. (**I**) High-resolution HAADF-STEM image of the J-PtNWs after ADT. The circled areas indicate defective regions with missing atoms. The inset shows the corresponding FFT image.

after the electrochemical dealloying process (Fig. 1C). The HRTEM images show that the overall diameter of the nanowire shrank from ~5.0 nm to ~2.2 nm after the CV cycles, with well-resolved lattice spacing of 0.23 nm, again consistent with Pt (111) (Fig. 1F). The EDX spectroscopy line scan showed that Pt was the only dominant element in the resulting nanowires (Fig. 1I), further confirming complete Ni leaching. In addition, the

CV scan of the fully activated nanowires (after 160 CV cycles) in 0.1 M KOH showed an absence of typical Ni^{2+}/Ni^{3+} redox signatures, in contrast to the partially activated (150 cycles) PtNi alloy nanowires in which the Ni^{2+}/Ni^{3+} redox peaks were prominent (fig. S6). We also conducted a CO-stripping experiment to determine the $ECSA_{CO}$ of J-PtNWs (fig. S7). The resulting ratio of $ECSA_{Hupd}$: $ECSA_{CO}$ is 1.00:1.05, which is in agreement with that

of typical pure Pt material (10). Furthermore, TEM studies of the dealloyed nanowires also showed a highly jagged surface (Fig. 1, C and F) with rich atomic steps, in contrast to the relatively smooth surface observed in typical synthetic PtNWs (fig. S1B). On the basis of these observations, we denote the resulting nanowires as J-PtNWs.

The electrocatalytic performance of the resulting nanowires was compared with a commercial

Fig. 3. Structural analysis of the J-PtNWs obtained from ReaxFF reactive molecular dynamics and x-ray absorption spectroscopy. (**A**) Pictorial illustrations of the final structure of a J-PtNW generated by reactive molecular dynamics simulations, with an average diameter of ~2.2 nm and length of ~46 nm. (**B**) J-PtNW with colored atoms to show the five-fold index. (**C**) J-PtNW with colored atoms to show distribution of atomic stress (in atm·nm^3). (**D**) Pt-Pt radial distribution function (RDF) of the SMA-predicted J-PtNW (red) compared with the peaks of the RDF for the regular PtNW (black). (**E**) Pt L$_3$ edge FT-EXAFS spectrum (black) collected ex situ and the corresponding first-shell least-squares fit (red) for the J-PtNWs. (**F**) Distribution of the absolute values of the average atomic stress on surface rhombi for the R-PtNWs (black) and the J-PtNWs (red). A rhombus is an ensemble of four atoms arranged as two equilateral triangles sharing one edge, as shown in the inset.
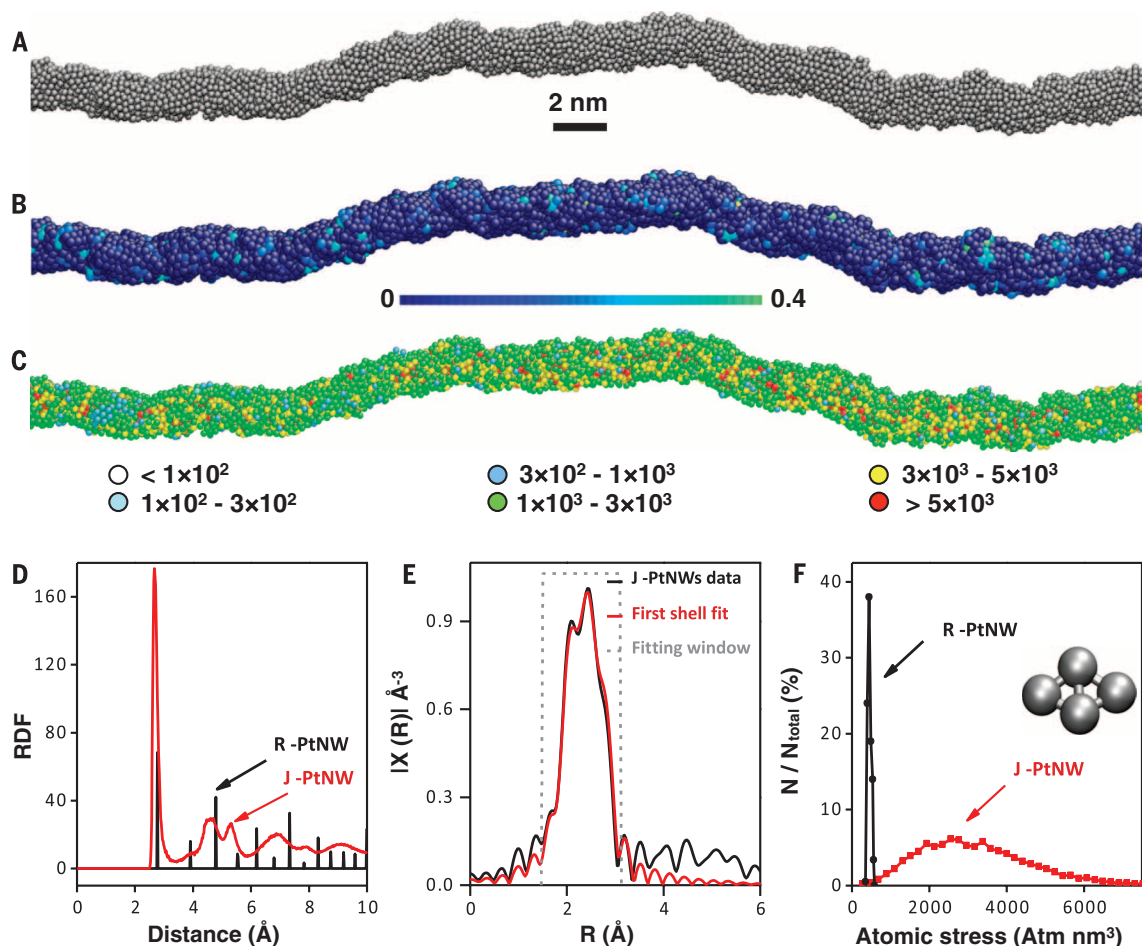
Pt/C catalyst (10% mass loading of ~3- to 5-nm Pt NPs on carbon support) and directly synthesized regular PtNWs (R-PtNWs, diameter ~1.8 nm; fig. S1B) with a relatively smooth surface (*25*). To assess ORR activity, we loaded all catalysts onto glassy carbon electrodes (Pt mass loading: 2.2 μg/cm^2 for J-PtNWs, 2.55 μg/cm^2 for R-PtNWs, and 7.65 μg/cm^2 for Pt/C catalyst). We used CV to measure the ECSA (Fig. 2C). Overall, the J-PtNWs, R-PtNWs, and Pt/C catalyst showed ECSA values of 118, 110, and 74 m^2/g$_{Pt}$, respectively (Table 1). The synthetic R-PtNWs also exhibited a rather high ECSA that may be related to their ultrasmall diameters (~1.8 nm).

Figure 2D shows the ORR polarization curves normalized by glassy carbon electrode geometric area (0.196 cm^2). The half-wave potential for the J-PtNWs was 0.935 V, which is considerably higher than those of the commercial Pt/C catalyst (0.86 V) and the R-PtNWs (0.90 V), suggesting excellent ORR activity of the J-PtNWs. The Koutecky-Levich equation was used to calculate the kinetic current by considering the mass-transport correction. The specific and mass activities were normalized by the ECSA or the total mass of the loaded Pt, respectively. Overall, the J-PtNWs showed a specific activity of 11.5 mA/cm^2 at 0.90 V versus RHE, far higher than 0.35 mA/cm^2 for the Pt/C catalyst or

1.59 mA/cm^2 for the R-PtNWs tested under the same conditions (Table 1). Together with their ultrahigh specific surface area, the J-PtNWs deliver a high mass activity of 13.6 A/mg$_{Pt}$ at 0.9 V versus RHE, which is 52 times that of the 10 weight percent Pt/C (0.26 A/mg$_{Pt}$) and more than 7 times that of the R-PtNWs (1.76 A/mg$_{Pt}$) (Fig. 2G and Table 1). The mass activity achieved in the J-PtNWs is nearly double the highest previously reported mass activity value of 6.98 A/mg$_{Pt}$ (*19*) and 5.7 A/mg$_{Pt}$ (*23*). This observed mass activity was highly reproducible and was between 10.8 and 13.8 A/mg$_{Pt}$ in >15 independently tested J-PtNW electrodes.

Because the current at 0.90 V is already near the diffusion-limited current in the ORR polarization curve, we also compared mass activity at half-wave potential of the J-PtNWs (0.935 V) in Table 1. Our analysis shows that the J-PtNWs still exhibited a mass activity 48 times that of the Pt/C catalyst. The Tafel plots of specific activity (Fig. 2E) exhibit slopes of 51, 72, and 74 mV decade^{-1} for the J-PtNWs, R-PtNWs, and Pt/C catalyst, respectively. A considerably smaller slope achieved in the J-PtNWs suggests significantly improved kinetics for ORR. Remarkably, the mass activity Tafel plot (Fig. 2F) shows that the J-PtNWs deliver mass activity 30 times the 2017 target set by

the U.S. Department of Energy (DOE) (0.44 A/mg$_{Pt}$ at 0.90 V for MEA, highlighted by purple dashed line in Fig. 2F). The J-PtNWs can deliver the DOE targeted mass activity at 0.975 V (RHE), thus reducing the overpotential by 0.075 V.

We evaluated the durability of the J-PtNWs using accelerated deterioration tests (ADT) under a sweep rate of 100 mV s^{-1} between 0.6 V and 1.0 V in O$_2$ saturated 0.1 M HClO$_4$. After 6000 cycles, the ECSA dropped by only ~7%, the specific activity dropped by only ~5.5%, and together the mass activity dropped by only 12% (Fig. 2H). The retention of high ECSA in J-PtNWs during ADT is in stark contrast to that of the Pt/C catalyst, which showed a much larger loss (~30%) in ECSA during similar ADTs. Ultrafine nanostructures (e.g., ~2 nm) have shown severely worse stability relative to their bulk counterpart (*26, 27*) due to movement, aggregation, and Ostwald ripening processes. The unique one-dimensional geometry of nanowires and the multipoint contacts with the carbon support might reduce such movement and aggregation, and might also deter the Ostwald ripening process usually observed in spherical NPs (fig. S8), thereby contributing to the excellent durability. Indeed, our TEM studies before and after ADT showed little change in the

overall morphology or size of the J-PtNWs on the carbon support (fig. S9). High-resolution STEM studies showed that the jagged surface (with defective sites) was largely preserved after 6000 cycles (Fig. 2I).

The above results demonstrate that the J-PtNWs exhibit ultrahigh specific surface area and specific activity, together delivering a record-high mass activity for ORR. Notably, the J-PtNWs exhibit considerably higher specific activity and mass activity (11.5 mA/cm^2 or 13.6 A/mg$_{Pt}$ at 0.9 V) than those of R-PtNWs (1.59 mA/cm^2 or 1.76 A/mg$_{Pt}$ at 0.9 V), despite similar ECSA values (118 m^2/g$_{Pt}$ for 2.2-nm J-PtNWs, 110 m^2/g$_{Pt}$ for 1.8-nm R-PtNWs). Relative to the Pt/C catalyst, the J-PtNWs show a factor of 33 increase in specific activity at 0.90 V versus RHE, which suggests that the activation energy for the rate-determining step of ORR on the J-PtNWs is reduced by 0.090 eV from that of the Pt/C catalyst [$\Delta E_{act} = k_B T \ln(SA_{J\text{-}PtNW}/SA_{Pt/C})$, where ΔE_{act} is the difference in activation energy, k_B is Boltzmann's constant, T is temperature, $SA_{J\text{-}PtNW}$ is the specific activity of J-PtNWs, and $SA_{Pt/C}$ is the specific activity of the Pt/C catalyst]. This decrease is plausible according to our various ORR computations (16).

To gain further insight on how the J-PtNWs could deliver substantially higher ORR activity, we conducted reactive molecular dynamics (RMD) studies using the reactive force field (ReaxFF) (28) to simulate the formation of J-PtNWs by leaching Ni atoms from initially Pt$_{15}$Ni$_{85}$ alloy nanowires (16), as well as a second moment approximation (SMA) tight-binding potential (29) for final local optimization and prediction of Pt-Pt distances (25). The RMD simulation resulted in a pure PtNW containing 7165 Pt atoms (in a length of ~46 nm) with a diameter of ~2.2 nm and a highly jagged surface (Fig. 3A). Notably, the overall morphology of the predicted J-PtNWs resembles closely the experimentally obtained J-PtNWs as shown in TEM images in Fig. 1, both of which show modulating thread-like segments ~2.2 nm in diameter containing striction regions, bending points, and jagged surfaces.

The predicted radial distribution function for the J-PtNW exhibits a well-defined first-neighbor peak at about 2.70 Å (Fig. 3D), which is ~2.2 to 2.5% shorter than the Pt-Pt first-neighbor distance predicted for the R-PtNWs (2.76 Å) and the bulk Pt crystal (2.77 Å), whereas the peaks associated with the second and farther neighbors are much broader and more blurred, similar to those reported in nanoporous NPs (16). These predicted Pt-Pt first-neighbor distances are well confirmed by the EXAFS analysis (Fig. 3E, fig. S10, and table S1), which reveals that the first-shell Pt-Pt bond length in the J-PtNWs (2.71 Å) is ~1.8% shorter than that of the Pt foil (2.76 Å).

Nanowires with small diameters (~2.2 nm in this case) inherently have ultrahigh surface area that can be further enhanced by the surface roughness of a jagged morphology. We calculated the van der Waals surface area of the simulated J-PtNWs to be ~110 m^2/g$_{Pt}$ (table S2), which agrees well with our experimental value derived from the ECSA (118 m^2/g$_{Pt}$). However, the enhancement

of surface area alone cannot fully account for the observed ORR mass activity. Stressed and undercoordinated crystalline-like surface rhombi can markedly decrease the reaction barrier of the rate-determining steps of ORR, thus improving specific ORR activity (16). Surface rhombi are ensembles of four atoms arranged as two equilateral triangles sharing one edge (see the inset in Fig. 3F) and resembling the triangular tessellation of an fcc (111) surface, which we find to be superior to a square tessellation for ORR activity in the same way that the fcc (111) surface is more ORR-active than other compact fcc surfaces such as fcc (100) (1, 30). Moreover, rhombi that are stressed and undercoordinated but still crystalline-like exhibit smaller overall energy barriers for ORR than those encountered on the rhombi of the fcc (111) surface, as predicted via density functional theory calculations (16).

Several factors could contribute to the greatly enhanced ORR activity in the J-PtNWs:

(i) Our analysis shows that the coordination number of surface atoms in the J-PtNWs ranges mostly between 6 and 8 (fig. S11A), indicating that these surface atoms are undercoordinated relative to typical crystal surfaces [with coordination numbers of 8 or 9 for (100) or (111) facets, respectively]. Despite the low coordination number and jagged features, the crystalline-like character of surface atoms in J-PtNWs is confirmed from common neighbor analysis (CNA) (31–33), which shows that the ratio of CNA [5, 5, 5] triplets (a marker of icosahedral structure) (29, 34) to the total number of CNA triplets is rather low (84% of the atoms have a ratio below 0.0065) (Fig. 3B). Because the bonded pairs of type [5, 5, 5] are characteristic of icosahedral order, this low [5, 5, 5] ratio indicates a more crystalline-like feature (32) for our established model, which is also a crucial factor for enhancing ORR activity (16). Indeed, such crystalline-like character in our simulation model is consistent with the experimental fast Fourier transform (FFT) images (insets in Fig. 1F and Fig. 2I) showing that the J-PtNWs remain fcc-like after CV activation and repeated cycling. Additionally, the distribution of rhombus dihedral angles (fig. S11B) shows that most of the dihedral angles formed between the two triangles of the rhombus are in the range of 156° to 180°. Given the 180° dihedral angle for typical crystalline Pt (111) facets, this statistical analysis further confirms the high-crystallinity nature of the J-PtNWs, which is favorable for increased reactivity (16).

(ii) The surface atoms in the J-PtNWs exhibit rather high values of Cauchy atomic stress times atomic volume, about 10 times that for regular (100) or (111) facets (Fig. 3, C and F), as also confirmed by simulated and EXAFS-derived Pt-Pt distances (Fig. 3, D and E). Moreover, the ReaxFF surface energy of the J-PtNW is 2.7 J/m^2, which exceeds the value for the Pt(111) surface (1.7 J/m^2; this latter ReaxFF value is in very good agreement with quantum mechanics and experimental values). This mechanical strain can decrease the binding energy of adsorbents on close-packed surfaces, which can make the surfaces more active (32, 35, 36), further contributing to the activity enhancement.

(iii) We found that the J-PtNWs possess a large ECSA (table S2) and also exhibit an unusually high number of the ORR-favorable rhombic structures on the surface. There are 76% rhombi per surface atom in the J-PtNW surface (table S2), considerably higher than the 57% previously reported for the nanoporous Pt-NPs (16).

Because Ni is sacrificial in the process of forming pure J-PtNWs, other sacrificial elements may also be selectively removed from their alloys through electrochemical, chemical, or thermal dealloying processes to result in jagged surfaces with improved catalytic activity. We also prepared similar J-PtNWs by electrochemical dealloying PtCo nanowires and achieved an ORR activity of 8.1 A/mg$_{Pt}$ (figs. S12 and S13), which exceeds the highest number reported previously (6.98 A/mg$_{Pt}$). We attribute the lower mass activity relative to PtNi-derived J-PtNWs to the slightly larger diameter of the resulting nanowires (~2.5 versus ~2.2 nm), leading to a smaller ECSA (92 m^2/g$_{Pt}$ versus 118 m^2/g$_{Pt}$) and possibly to differences in the dealloying mechanism of Co with respect to Ni. These studies further demonstrate the validity and generality of our approach to deriving highly ORR-active J-PtNWs from alloy nanowires.

REFERENCES AND NOTES

1. V. R. Stamenkovic et al., Science 315, 493–497 (2007).
2. N. S. Porter, H. Wu, Z. Quan, J. Fang, Acc. Chem. Res. 46, 1867–1877 (2013).
3. J. Wu, H. Yang, Acc. Chem. Res. 46, 1848–1857 (2013).
4. Y. J. Wang et al., Chem. Rev. 115, 3433–3467 (2015).
5. Z. Peng, H. Yang, Nano Today 4, 143–164 (2009).
6. D. Wang et al., Nat. Mater. 12, 81–87 (2013).
7. C. Wang et al., Adv. Funct. Mater. 21, 147–152 (2011).
8. D. F. van der Vliet et al., Nat. Mater. 11, 1051–1058 (2012).
9. V. R. Stamenkovic et al., Nat. Mater. 6, 241–247 (2007).
10. D. F. van der Vliet et al., Angew. Chem. Int. Ed. 51, 3139–3142 (2012).
11. C. Cui, L. Gan, M. Heggen, S. Rudi, P. Strasser, Nat. Mater. 12, 765–771 (2013).
12. V. R. Stamenkovic, B. S. Mun, K. J. J. Mayrhofer, P. N. Ross, N. M. Marković, J. Am. Chem. Soc. 128, 8813–8819 (2006).
13. V. Calle-Vallejo, J. I. Martínez, J. M. García-Lastra, P. Sautet, D. Loffreda, Angew. Chem. Int. Ed. 53, 8316–8319 (2014).
14. F. Calle-Vallejo et al., Science 350, 185–189 (2015).
15. M. Escudero-Escribano et al., Science 352, 73–76 (2016).
16. A. Fortunelli et al., Chem. Sci. 6, 3915–3925 (2015).
17. S. Choi et al., Nano Lett. 13, 3420–3425 (2013).
18. X. Huang et al., Energy Environ. Sci. 7, 2957–2962 (2014).
19. X. Huang et al., Science 348, 1230–1234 (2015).
20. H. Zhu, S. Zhang, S. Guo, D. Su, S. Sun, J. Am. Chem. Soc. 135, 7130–7133 (2013).
21. S. Guo et al., Angew. Chem. Int. Ed. 52, 3465–3468 (2013).
22. L. Zhang et al., Science 349, 412–416 (2015).
23. C. Chen et al., Science 343, 1339–1343 (2014).
24. S. Zhang et al., J. Am. Chem. Soc. 136, 15921–15924 (2014).
25. See supplementary materials on Science Online.
26. L. Tang et al., J. Am. Chem. Soc. 132, 596–600 (2010).
27. L. Tang, X. Li, R. C. Cammarata, C. Friesen, K. Sieradzki, J. Am. Chem. Soc. 132, 11722–11726 (2010).
28. C. F. Sanz-Navarro et al., J. Phys. Chem. A 112, 1392–1402 (2008).
29. F. Cleri, V. Rosato, Phys. Rev. B 48, 22–33 (1993).
30. Y. Sha, T. H. Yu, B. V. Merinov, P. Shirvanian, W. A. Goddard III, J. Phys. Chem. Lett. 2, 572–576 (2011).
31. D. Faken, H. Jonsson, Comput. Mater. Sci. 2, 279–286 (1994).
32. S. Schnur, A. Groß, Phys. Rev. B 81, 033402 (2010).
33. J. D. Honeycutt, H. C. Andersen, J. Phys. Chem. 91, 4950–4963 (1987).

34. A. Stukowski, *Model. Simul. Mater. Sci. Eng.* **20**, 045021 (2012).
35. M. F. Francis, W. A. Curtin, *Nat. Commun.* **6**, 6261 (2015).
36. S. Zhang *et al.*, *J. Am. Chem. Soc.* **136**, 7734–7739 (2014).

TORNADOES

More tornadoes in the most extreme U.S. tornado outbreaks

Michael K. Tippett,[1,2]* Chiara Lepore,[3] Joel E. Cohen[4,5,6]

Tornadoes and severe thunderstorms kill people and damage property every year. Estimated U.S. insured losses due to severe thunderstorms in the first half of 2016 were $8.5 billion (US). The largest U.S. effects of tornadoes result from tornado outbreaks, which are sequences of tornadoes that occur in close succession. Here, using extreme value analysis, we find that the frequency of U.S. outbreaks with many tornadoes is increasing and that it is increasing faster for more extreme outbreaks. We model this behavior by extreme value distributions with parameters that are linear functions of time or of some indicators of multidecadal climatic variability. Extreme meteorological environments associated with severe thunderstorms show consistent upward trends, but the trends do not resemble those currently expected to result from global warming.

In the United States, tornado outbreaks have substantial effects on human lives and property. Tornado outbreaks are sequences of six or more tornadoes that are rated F1 and greater on the Fujita scale or rated EF1 and greater on the Enhanced Fujita scale and that occur in close succession (*1*, *2*). About 79% of tornado fatalities during the period 1972 to 2010 occurred in outbreaks (*1*), and 35 people died in U.S. tornado outbreaks in 2015. No significant trends have been found in either the annual number of reliably reported tornadoes (*3*) or of outbreaks (*1*). However, recent studies indicate increased variability in large normalized economic and insured losses from U.S. thunderstorms (*4*), increases in the annual number of days on which many tornadoes occur (*3*, *5*), and increases in the annual mean and variance of the number of tornadoes per outbreak (*6*). Here, using extreme value analysis, we find that the frequency of U.S. outbreaks with many tornadoes is increasing and that it is increasing faster for more extreme outbreaks. We model this behavior by extreme value distributions with parameters that are linear functions of time or of some indicators of multidecadal climatic variability. Extreme meteorological environments associated with severe thunderstorms show consistent upward trends, but the trends do not resemble those currently expected to result from global warming.

Linear trends in the percentiles of the number of tornadoes per outbreak (Fig. 1A) are positive, statistically significant, and increase exponentially faster with percentile probability (Fig. 1B). This behavior is consistent with the positive trends in

[1]Department of Applied Physics and Applied Mathematics, Columbia University, New York, NY, USA. [2]Center of Excellence for Climate Change Research, Department of Meteorology, King Abdulaziz University, Jeddah, Saudi Arabia. [3]Lamont Doherty Earth Observatory, Columbia University, Palisades, NY 10964, USA. [4]Laboratory of Populations, Rockefeller University, New York, NY 10065, USA. [5]The Earth Institute and Department of Statistics, Columbia University, New York, NY 10027, USA. [6]Department of Statistics, University of Chicago, Chicago, IL 60637, USA.
*Corresponding author. Email: mkt14@columbia.edu
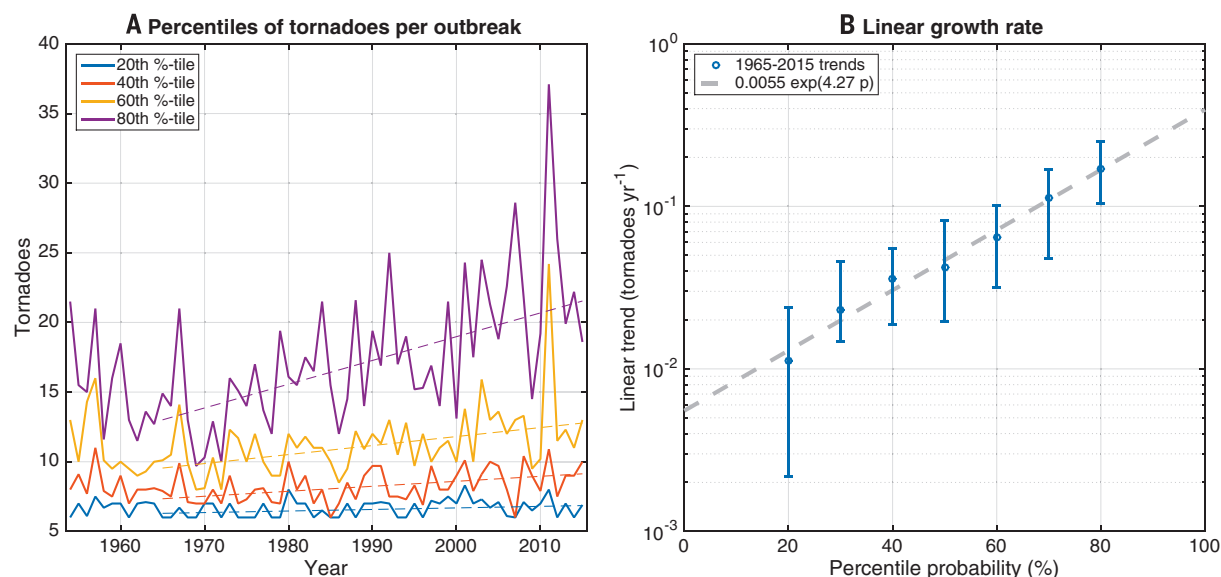
Fig. 1. Numbers of tornadoes per outbreak. (**A**) Annual 20th, 40th, 60th, and 80th percentiles of the number of E/F1+ tornadoes per outbreak (6 or more E/F1+ tornadoes), 1954 to 2015 (solid lines), and quantile regression fits to 1965 to 2015, assuming linear growth in time (dashed lines). (**B**) Linear growth rates as a function of percentile probability. Error bars are 95% bootstrap confidence intervals and indicate linear trends that are statistically significantly different from zero.

Science

An activity lift for platinum

Platinum is an excellent but expensive catalyst for the oxygen reduction reaction (ORR), which is critical for fuel cells. Alloying platinum with other metals can create shells of platinum on cores of less expensive metals, which increases its surface exposure, and compressive strain in the layer can also boost its activity (see the Perspective by Stephens *et al.*). Bu *et al.* produced nanoplates—platinum-lead cores covered with platinum shells—that were in tensile strain. These nanoplates had high and stable ORR activity, which theory suggests arises from the strain optimizing the platinum-oxygen bond strength. Li *et al.* optimized both the amount of surface-exposed platinum and the specific activity. They made nanowires with a nickel oxide core and a platinum shell, annealed them to the metal alloy, and then leached out the nickel to form a rough surface. The mass activity was about double the best reported values from previous studies.

Science, this issue p. 1410, p. 1414; see also p. 1378

ARTICLE TOOLS	http://science.sciencemag.org/content/354/6318/1414
SUPPLEMENTARY MATERIALS	http://science.sciencemag.org/content/suppl/2016/11/16/science.aaf9050.DC1
RELATED CONTENT	http://science.sciencemag.org/content/sci/354/6318/1378.full http://science.sciencemag.org/content/sci/354/6318/1410.full
REFERENCES	This article cites 38 articles, 6 of which you can access for free http://science.sciencemag.org/content/354/6318/1414#BIBL
PERMISSIONS	http://www.sciencemag.org/help/reprints-and-permissions

Use of this article is subject to the Terms of Service